



# AMERICAN METEOROLOGICAL SOCIETY

*Monthly Weather Review*

## EARLY ONLINE RELEASE

This is a preliminary PDF of the author-produced manuscript that has been peer-reviewed and accepted for publication. Since it is being posted so soon after acceptance, it has not yet been copyedited, formatted, or processed by AMS Publications. This preliminary version of the manuscript may be downloaded, distributed, and cited, but please be aware that there will be visual differences and possibly some content differences between this version and the final published version.

The DOI for this manuscript is doi: 10.1175/2008MWR2754.1

The final published version of this manuscript will replace the preliminary version at the above DOI once it is available.



# Airflow and Precipitation Properties within the Stratiform Region of Tropical Storm Gabrielle during landfall

Dong-Kyun Kim, Kevin R. Knupp

*Department of Atmospheric Sciences, University of Alabama in Huntsville*

*320 Sparkman Dr. Huntsville AL 35806 USA*

Christopher R. Williams<sup>1</sup>

<sup>1</sup>*Cooperative Institute for Research in Environmental Sciences, University of Colorado at  
Boulder, Boulder, Colorado, USA*

Submitted to Monthly Weather Review

Revised November 2008

---

Corresponding author: Dong-Kyun Kim, Department of Atmospheric Sciences, University of Alabama in Huntsville,  
Huntsville, AL 35816. Email: [dkkim@nsstc.uah.edu](mailto:dkkim@nsstc.uah.edu)

## ABSTRACT

Kinematic and microphysical characteristics of a stratiform rainband within Tropical Storm Gabrielle during landfall on 14 September 2001 were investigated using data from a co-located 915-MHz wind profiler and scanning Doppler radar. The curved 60 km wide rainband was relatively intense with mesoscale updrafts and downdrafts exceeding  $\pm 1 \text{ m s}^{-1}$ . The bright band is classified as strong, as indicated by reflectivity factors in excess of 50 dBZ and rainfall rates below the bright band peaking at 10-20  $\text{mm hr}^{-1}$ . The melting layer microphysical processes were examined to understand the relation between bright band processes and precipitation intensity and kinematics (mesoscale downdraft in particular) below the melting layer.

The profiler and Doppler radar analyses, designed to maximize vertical resolution of flows within the melting layer, disclose a striking convergence-divergence couplet through the melting layer that implies a prominent cooling-induced fine-scale circulation. Melting-driven cooling initiates mid-level convergence in the upper part of the melting region, while weak convergence to positive divergence is analyzed within the lower melting layer. A melting layer parameter study indicates the significance of the level of maximum reflectivity that separates convergence above from divergence below, and also reveals a mixture of aggregation and breakup of ice particles, with aggregation being dominant.

In this vigorous rainband case, the presence of strong mesoscale downdrafts cannot be ignored for accurate retrievals of raindrop size distribution (RSD) and precipitation parameters from the Sans Air Motion (SAM) model. When downdrafts are included, retrieved rainfall estimates were much higher than those under the zero vertical air motion assumption, and were slightly less than those from a power law  $Z$ - $R$  relation. The rainfall estimates show a positive

correlation with reflectivity factor and bright band intensity (i.e., aggregation degree) but less dependence on bright band height.

## 1. Introduction

Stratiform precipitation within tropical cyclones (TCs) is significant due to its relatively large aerial coverage and contribution to the total water budget and associated latent heating (Gamache et al. 1993; Schumacher and Houze 2003). The microphysics and dynamics within stratiform regions of TCs must be understood within the context of vertical air motions that account for the hydrometeor growth and size distribution evolution above, within, and below the melting layer. As an important part of water phase transitions, the melting layer can affect stratiform dynamics and TC intensity.

Willis and Heymsfield (1989) noted that the 0 °C isothermal layer formed by melting produces a transition layer that separates dynamics above and below the melting layer. They observed vertical wind fluctuations due to the pressure and buoyancy changes produced by melting-driven cooling. Using a mesoscale model, Szeto et al. (1988) indicated that melting-driven cooling can have large impacts on the circulations near the melting layer by perturbing thermal and dynamic fields. Since this cooling is concentrated in a narrow melting zone, cooling by melting of snow particles may be more significant in producing mesoscale downdrafts than evaporational cooling from raindrops (Srivastava 1987). Enhanced mesoscale downdrafts can transport low-valued  $\theta_e$  air downwards and decrease the temperature within the boundary layer (Yang et al. 2007). Such downdrafts processes require close examination in view of the potential impact on TC intensity (Barnes et al. 1983; Powell 1990).

Two important microphysical processes around the melting layer are snow aggregation in the upper portion of the melting layer, and breakup within the lower part of the melting layer (Klaassen 1988; Yokoyama et al. 1985). The bright band is an important radar feature since changes in precipitation rate and raindrop size distribution (RSD) are closely related to bright

band intensity and its dependence on aggregation and breakup. However, only a limited number of studies have used a vertically pointing wind profiler to examine the melting layer microphysics and dynamics within stratiform precipitation (Drummond et al. 1996; Fabry and Zawadzki 1995; Huggel et al. 1996; Zawadzki et al. 2005). To our knowledge, such studies in stratiform precipitation of TCs have not been conducted.

As a different aspect from a recent study of Tropical Storm (TS) Gabrielle (Knupp et al. 2006), we focus on the dynamical and microphysical properties around the melting layer. The primary goal of this study is to investigate the microphysical and kinematic properties of the melting layer and its impact on mesoscale downdrafts and precipitation properties below the melting layer. This paper is organized as follows. In Section 2 we describe the instruments and Doppler radar techniques utilized to derive vertical air motion and horizontal divergence. In Section 3, the evolution and environmental features of TS Gabrielle is addressed. In Sections 4 and 5, we examine the dynamical and microphysical properties around the melting layer based on a quantitative parameter analysis and various radar analysis techniques described in Section 2. These sections also investigate the temporal and vertical variations of the RSDs and discuss their characteristics via the RSD parameters, particularly during aggregation and breakup-dominant periods. A discussion and conclusions follow in Section 6 and Section 7, respectively.

## **2. Instrumentation and analysis techniques**

Primary instruments used in this study were the 915-MHz wind profiler of the Mobile Integrated Profiling System (MIPS), the Shared Mobile Atmosphere Research and Teaching Radar (SMART-R), and the Tampa Bay WSR-88D (TBW) radar. The 915-MHz wind profiler sampled from five beams, one vertical and four orthogonal beams with off vertical angle of 23.6

degrees. The dwell time for each beam was about 30 s and the range gate spacing was 105 m with high-height mode. The vertical beam measurement was sampled every 60 s. The SMART-R is a mobile C-band Doppler radar (Biggerstaff et al. 2005), which sampled volumes consisting of 17 elevation angles from 1.8 to 44.3 degrees over 5-min intervals during the 0545-0648 UTC period. The TBW radar located 70 km north of the SMART-R was used to analyze the horizontal and vertical structure of TS Gabrielle (see Fig. 1).

*a. Analysis techniques*

Four different methods were used for obtaining vertical air motion; 1) reflectivity-fall speed relationships, 2) Extended Velocity Azimuth Display (EVAD), 3) Quasi-Velocity Azimuth Display (Q-VAD), and 4) Sans Air Motion (SAM) model (discussed in subsection b). The EVAD, Q-VAD, and the divergence theorem were used to determine horizontal divergence. Vertical air motion ( $w$ ) is estimated using the reflectivity-fall speed relations for rain (Ulbrich and Chilson 1994) and for snow (Atlas et al. 1973)

$$w = W_{dop} - 3.5Z_{rain}^{0.084} (\rho_0 / \rho)^{0.4} \quad (\text{rain}) \quad (1)$$

$$w = W_{dop} - 0.81Z_{snow}^{0.063} (\rho_0 / \rho)^{0.4} \quad (\text{snow}), \quad (2)$$

where  $Z_{rain}$  and  $Z_{snow}$  are radar reflectivity factors ( $\text{mm}^6 \text{m}^{-3}$ ) for rain and snow, respectively,  $w$  is vertical air motion, and  $W_{dop}$  is mean Doppler velocity at vertical incidence measured by the wind profiler. Both  $w$  and  $W_{dop}$  are negative downward. The term  $(\rho_0 / \rho)^{0.4}$  is the atmospheric density correction (Beard 1985), where  $\rho$  is air density parameterized by  $\rho(z) = \rho_0 \exp(-z/9.58)$  and  $z$  is altitude in km. The two relationships were applied to pure snow and rain regions separated by the snow and rain levels defined at the maximum curvature in the  $Z$  profile. For the intermediate layer

between the snow and rain levels,  $w$  was acquired by performing a linear interpolation between the values within the rain and overlying snow levels.

The EVAD provides profiles of  $w$ , terminal fall velocity, and horizontal divergence by processing data at horizontal rings in all elevation cones per layer (Matejka and Srivastava 1991). The EVAD performs a linear regression using the equation

$$\frac{2a_o}{r \cos \alpha} = div + W_{dop} \frac{2 \sin \alpha}{r \cos \alpha}, \quad (3)$$

where  $div$  is horizontal divergence,  $W_{dop}$  is Doppler velocity,  $\alpha$  is the elevation angle,  $r$  is the radius of the VAD circle, and  $a_o$  is the zeroth harmonic coefficient as a function of the radius and elevation angle. Two unknowns,  $div$  (intercept) and  $W_{dop}$  (slope) per layer are determined by the linear regression between the X and Y terms (i.e.,  $Y = aX + b$ ) in (3). After a  $div$  profile is obtained from the regression, a  $w$  profile is produced by performing a variational integration of the mass continuity equation. One important assumption is that the wind field over the analysis domain is horizontally linear. Also divergence and terminal fall velocity for a given layer are considered as homogeneous over the maximum horizontal range of the rings.

The Q-VAD computes the wind gradient using two opposite beams of the 915-MHz profiler. The vertical air motion, assumed to be identical over all five beams at the same time, is derived from downward integration of the anelastic continuity equation starting with EVAD vertical air motion as the top boundary condition ( $w_{top}$ )

$$w_{k-m} = w_{top} + \sum_{i=k-m}^k div_i \Delta z_i \quad (m = 0 \dots k), \quad (4)$$

where  $div$  is the sum of  $\Delta u / \Delta x$  and  $\Delta v / \Delta y$ , the east-west and north-south gradients of the winds divided by a horizontal distance between the off-vertical range gates of the two beams. Divergence estimates become increasingly noisy at low levels because the horizontal distance



between the opposite beams decreases with decreasing height. Thus,  $div$  and  $w$  from the QVAD technique are not displayed below 2 km AGL.

The divergence theorem was utilized to estimate  $div$  using the highest elevation angle (44.2 degree) of the SMART-R. This technique has been used to diagnose diabatic  $div$  profiles in tropical mesoscale convective systems (MCSs) using aircraft radar measurements (Mapes and Houze 1993, 1995). This highest elevation angle was selected to most closely match the sampling volume of the 915-MHz profiler. The horizontal divergence over an area  $A$  is equal to the closed line integral of the normal component of Doppler radial velocity ( $V_r$ ) shown by

$$\frac{1}{A} \int \nabla \cdot V dA = \frac{1}{A} \oint V_h dl, \quad (5)$$

where  $V_h$  is a horizontal component of  $V_r$  and  $dl$  is a length element along the circular boundary.

The horizontal component ( $V_h$ ) of Doppler radial velocity is calculated by

$$V_h = V_r \sec \theta - (w - V_f) \tan \theta, \quad (6)$$

where  $V_f$  is the terminal fall speed expressed with positive values for upward motion to match the vertical air motion sign convention.

*b. Sans Air Motion (SAM) Model – the non-zero vertical air motion*

The RSDs and their integral parameters such as rain rate and liquid water content can be retrieved from the Doppler velocity power spectrum of wind profiler radars. In doing this,  $w$ , turbulence, noise level, and deviation of Rayleigh scattering need to be taken into account. In this study, the Sans Air Motion (SAM) model (Williams 2002) is used to retrieve the RSDs below the melting layer in the stratiform rainband. The retrieved RSDs are approximated by the gamma size distribution of the form

$$N(D) = N_0 D^\mu \exp(-\Lambda D), \quad (7)$$

where  $N(D)$  is the number concentration of particles which diameters range between  $D$  and  $D+dD$ .  $N_0$  ( $\text{m}^{-3} \text{mm}^{-1}$ ),  $\mu$ , and  $\Lambda$  ( $\text{mm}^{-1}$ ) are the intercept, shape, and slope parameters of the size distribution, respectively. The SAM model retrieves the hydrometeor spectrum by comparing the observed Doppler spectrum with many modeled spectra with the final retrieved spectrum minimizing a least square difference cost function. The modeled Doppler velocity spectrum is formed by convolving the clear-air spectrum with the modeled hydrometeor spectrum. The shape of modeled hydrometeor spectrum is varied by changing the mean mass-weighted diameter ( $D_m$ ) and  $\mu$ , and the clear-air spectrum by changing the clear-air mean vertical air velocity ( $w$ ) and spectral broadening ( $\sigma_{air}$ ). Rainfall rate is calculated from the three parameters ( $N_0$ ,  $D_m$  (or  $\Lambda$  using  $\Lambda=(4+\mu)/D_m$ ), and  $\mu$ ) of the gamma RSD by using

$$R(\text{mm hr}^{-1}) = \frac{6\pi}{10^4} \frac{N_0 \Gamma(4 + \mu)}{\Lambda^{(4+\mu)}} \left[ 9.65 - 10.3 \left( 1 + \frac{0.6}{\Lambda} \right)^{-(4+\mu)} \right], \quad (8)$$

To account for different vertical air motions, the SAM model uses a two step process. The first step estimates the best hydrometeor spectrum ( $N_0$ ,  $D_m$ , and  $\mu$ ) and spectral broadening ( $\sigma_{air}$ ) for a fixed vertical air velocity ( $w$ ) by minimizing the squared difference between the modeled and observed spectra. The first step is then repeated for many different vertical air motions. Values of  $w$  are acquired by shifting the observed spectrum along the velocity axis in one spectral bin increment ( $\Delta v=0.169 \text{ m s}^{-1}$ ) removing the effects of updrafts or downdrafts on the observed spectrum. As shifting the observed spectrum by a spectral bin increment, the best-fit hydrometeor spectrum with the final estimate of  $w$ , as a multiplication of the increment, is determined with the minimum cost function between the observed spectrum and the modeled spectrum. Shifting the

observed spectrum to account for updrafts decreases rainfall rates, whereas shifting the observed spectrum to account for downdrafts increases rainfall rates (Rajopadhyaya et al. 1998).

### **3. Tropical Storm Gabrielle**

#### *a. Storm evolution and environment*

Gabrielle was first classified as a tropical depression at 1800 UTC 11 September 2001 and attained a tropical storm status at 1200 UTC 13 September over the western Gulf of Mexico (Lawrence and Blake 2002; Molinari et al. 2006). Gabrielle then moved northeastward after 0000 UTC 14 September. A continuous intensification was observed for the next 12 hrs, particularly between 0600 and 1200 UTC, the time of landfall (Molinari et al. 2006). The MIPS, SMART-R, and TBW radar sampled an extensive stratiform rainband between 0430 and 0700 UTC. The storm circulation center was located southwest (upshear) of center of the stratiform rainband. During this period Gabrielle became more organized, as the deep convection (lower part of Fig. 1) intensified near the circulation center. The arc-shaped stratiform rainband (Fig. 1) appeared at around 0400 UTC and persisted until 1100 UTC. This rainband exhibited an arc length of ~250 km and a mean width of ~60 km.

A pronounced bright band signature was observed by the 915-MHz profiler and the TBW radar between 0500 and 0650 UTC. In Fig. 2, vertical sections of reflectivity factor and radial velocity at 0601 and 0656 UTC from the TBW radar, located 70 km north of the MIPS, show an extensive bright band near 4 km AGL. The increase in magnitudes of radial velocity, and vertical gradients in radial velocity near and above 6 km AGL reveal large vertical wind shear within the ice region at 0656 UTC, consistent with the findings of Molinari et al. (2006). Fig. 2e depicts a

cyclonic flow of about  $15 \text{ m s}^{-1}$  magnitude along the rainband in the dual Doppler analysis at 3.5 km AGL.

Two soundings were taken at 0000 and 0600 UTC from Tampa Bay (KTBW) within the stratiform precipitation (Fig. 3). At 0000 UTC, the 650-950 hPa layer is nearly saturated. The 0600 UTC sounding released near the leading edge of the rain band shows a slightly subsaturated layer (RH=85%) centered near 850 mb. This relatively unstable layer is between 770 and 850 hPa where mesoscale downdrafts are likely maintained by evaporational cooling. The extended saturated layer down to 770 hPa (2.2 km) at 0600 UTC could be ascribed to heat and moisture transport, supported by increased winds from the southeast direction (see the wind barbs on the right).

At 0600 UTC, it should be noted that an increase in temperature and wind speed occurred in the 500-800 hPa layer for the 6-hr period. Cooling within and below the melting layer is probably counteracted by heat and moisture transport from the south and southeast at these levels. Comparison with the 0000 UTC sounding reveals that cooling at low-levels was associated with the off-shore easterly flow. Knupp et al. (2006) noted that an extensive region of cool air at the surface preceded landfall and that the surface cold air exerted large effects on the ABL, and apparently on storm intensity changes. This cooling and its association with rainfall evaporation, mesoscale downdrafts, and precipitation properties is a primary motivation for this study.

*b. Overview of 915 MHz profiler measurements*

In Fig. 4a, the 915 MHz profiler-derived reflectivity factor ( $Z$ ) patterns show a prominent and continuous bright band signature whose height oscillated by  $\sim 200 \text{ m}$  from a mean height of 4.3 km. Rainfall rates up to  $23 \text{ mm hr}^{-1}$  and low-level  $Z$  maxima approaching 40 dBZ were

measured within this rainband. Within the melting layer near 4.2 km AGL,  $Z$  values exceeded 50 dBZ. These observations indicate that this was a relatively intense stratiform rainband. In Fig. 4b, the larger  $W_{dop}$  regions reaching about  $10 \text{ m s}^{-1}$  located particularly just below the stronger bright band, were well correlated with the regions of higher  $Z$  streaks around 0550, 0610, 0625, and 0635 UTC. A positive correlation between  $W_{dop}$  and  $Z$  and an increase in their magnitudes over several kilometers above the melting layer, particularly around 0550, 0625, and 0635 UTC, indicates a substantial increase in snow aggregation close to  $0^\circ\text{C}$  level.

In Fig. 4c, spectral widths show a notable contrast between the rain and ice regions except for thin layers of large spectral width near the bright band. The large spectral widths exceed about  $4.5 \text{ m s}^{-1}$  and are centered near 4.7 km, which appears to be a consequence of wide distributions in fall speeds of snow aggregates. The narrow region of small spectral widths less than  $2 \text{ m s}^{-1}$  near the level of maximum  $Z$  (4.0-4.5 km) between 0535 and 0645 UTC suggests much less breakup and more uniform distributions of fall speeds relative to that at the top of the melting layer. The  $w$  patterns and precipitation characteristics of this rainband are examined in greater detail in the following sections.

#### 4. Mesoscale flows

The SMART-R sampled the stratiform rainband with thirteen full volume scans from 0545 to 0650 UTC. During this period, horizontal winds over the SMART-R location ( $x=-4 \text{ km}$  and  $y=0 \text{ km}$  in Fig. 2e) were sufficiently uniform from the east-southeast so that the EVAD could be applied. The radius of the EVAD circle was set to 25 km.

In Fig. 5,  $w$  from the EVAD and 915-MHz profiler show similar structure. The profiler  $w$ , estimated from  $w_{915} = W_{dop} - V_f$  where  $V_f$  was derived from Eqs. 1 and 2, shows stronger up- and

downdrafts exceeding  $\pm 1 \text{ m s}^{-1}$ . Both the EVAD and  $w_{915}$  exhibit a lowering of the  $w = 0$  level during the period. Houze (1989) observed that the height of zero vertical air motion can vary from 0 to 2 km above the  $0^\circ\text{C}$  level, depending on location of the mean  $w$  profiles within stratiform regions. The lowering of the  $w = 0$  may be related to the increase in sampling the edges of the arc-shaped stratiform region as time progresses. Hence, irregularities in  $w$  increase in upper levels (i.e., above 8 km AGL in Fig. 5b). The greatest  $w_{915}$  downdraft magnitudes ( $-1.5 \text{ m s}^{-1}$ ) were analyzed below the melting layer from 0555 to 0610 UTC, earlier than those in the EVAD analysis (Fig. 5a). The slight mismatch in downdraft location between the two  $w$  fields may be attributed to the large difference in spatial resolution between the SMART-R (radius of 25 km) and the 915-MHz profiler.

Fig. 6 shows the  $div$  and  $w$  profiles from the EVAD, Q-VAD, and divergence theorem averaged over the 0545-0631 UTC period. All the  $div$  profiles show good agreement above the melting layer. Particularly, the  $div$  profiles from the Q-VAD and the divergence theorem are in better agreement despite a difference in the sampling domains between the profiler and the SMART-R at the maximum  $44.2^\circ$  elevation angle. The horizontal diameter for the divergence theorem at 10 km AGL at this angle is 19.5 km, more than two times greater than the 8.7 km distance between opposing beams in the Q-VAD at the same level. Since the divergence theorem utilizes the highest elevation angle ( $44.2^\circ$ ), the divergence error becomes larger at low altitudes. For this reason, the convergence magnitudes increase rapidly below 2 km AGL.

The composite  $div$  profile from the divergence theorem was a useful supplement to the composite Q-VAD divergence to examine small scale variations in airflow around the melting layer. In Fig. 6a, the convergence-divergence couplet in the Q-VAD  $div$  profile is notable between the  $0^\circ\text{C}$  level (4.8 km AGL) and 3.5 km AGL. Mapes and Houze (1995) attributed the

couplet to a warm-cold-warm temperature anomaly due to melting, suggesting that the convergence-divergence couplet is a result of a response to cold temperature perturbations within and warm temperature perturbation below the melting layer. The latter might be associated with adiabatic warming induced by subsidence. In addition, as melting-driven cooling strengthens mid-level convergence, weak convergence, near-zero or even positive divergence beneath it may occur to fulfill a mass balance in the vertical.

The *div* profile from the theorem shows a similar pattern but its variation is narrower than that of the Q-VAD. The difference in the *div* profiles between the Q-VAD and the divergence theorem near levels exhibiting a local maximum in divergence (e.g., near 3.7, and 2.5 km AGL) may be influenced by the terminal fall speed bias based on the  $Z-V_f$  relations and the decrease in range. The discrepancy is also a consequence of the difference in the sampling volumes of the two techniques. On the other hand, the EVAD *div* profile from the largest sampling volume shows better agreement with two other profiles above the melting layer, than below the melting layer. The vertical air motions from the three methods are in better agreement above the melting layer. The  $w_{915}$  profile reveals larger magnitudes above 6.5 km AGL, which is most likely due to the small sample volume.

## **5. Precipitation properties**

### *a. Melting layer and bright band signatures*

In Fig. 7a, the CFAD (Contoured Frequency by Altitude Diagram, Yuter and Houze 1995) of almost constant  $Z$  in the rain layer is shown with a strong bright band above during the 0530-0648 UTC period. Particularly, the  $Z$  CFAD shows a slight increase below 2 km AGL. The almost constant  $Z$  profiles are often measured in tropical stratiform regions (Cifelli et al. 2000;

Schumacher and Houze 2003; Tokay et al. 1999) as a result of the compensation between breakup of large drops and continuous collection of small drops, which maintain a constant  $Z$  (Huggel et al. 1996). Figs. 7a and 7b show a narrow distribution in both  $Z$  and  $W_{dop}$  from the top of the melting layer (4.8 km) to about 5.5 km AGL, suggesting that aggregation, accretion, and deposition processes at these levels comprise equilibrium in snow size spectra. The CFAD of  $W_{dop}$  shows relatively high frequencies centered near  $2 \text{ m s}^{-1}$  over a 1 km depth above the melting layer, implying that the mean fall speeds are independent of particle size and shape. However, as snow aggregates start melting, their size and fall velocity distributions become wider because the probability of collision rapidly increases at the same time. It is noted that an increase in the vertical gradients of  $W_{dop}$  is smaller in the upper part of melting layer than in the lower part because of a slower increase in melted fraction of snow in the upper part.

Spectral widths for snowflakes are narrower than those for raindrops since the range of fall speeds of snowflakes is smaller. But this range of fall speeds rapidly broadens as snow particles aggregate near the  $0^\circ\text{C}$  level where collision efficiency is relatively high. Large spectral widths near the top of the melting layer (Fig. 7c) are attributed to broader distributions of fall speeds of melting snow aggregates and perhaps to small-scale turbulence triggered by melting-driven cooling. However, an uncertainty still exists in the spectral width values obtained from the 915-MHz profiler observations as the spectra above the melting layer are more asymmetric with smaller peak values than those below the melting layer. One or both edges of the spectrum may be too steep, the spectral peak may be off-center, or the number of spectral peaks may be greater than one (Janssen and Van der Spek 1985). The increase in vertical wind shear (not shown) may have played a role on very asymmetric shapes (including some noise) of spectra near the top of the melting layer.



The CFADs for spectral widths and wind speeds (Figs. 7c and 7d) show a slow increase from 5 km AGL to near the 0 °C level. The heights of high spectral widths and large horizontal winds are almost identical near the top of the melting layer, suggesting that the increase in spectral widths is partially due to increased horizontal wind speed and wind shear.

The smallest spectral width values near the level of maximum  $Z$  (i.e., 4.4 km in Fig. 7a) suggest a minimum in breakup and a maximum in collection efficiency. Right below the levels of the  $Z$  maxima, the spectral widths rapidly increase, indicating that collisional breakup becomes more significant since the range of particle fall speeds in the lower half of the melting layer is, on average, larger due to partly or completely melted particles than in the upper half (Barthazy et al. 1998). Higher collision efficiency due to a larger range of fall speeds may produce more efficient breakup in the lower half of the melting layer. The second peak in the CFAD for spectral widths near 3.8 km may be attributed to increased instability associated with cooling (i.e., increased lapse rate of air temperature) as well as mixed distributions of raindrops and partially melted particles near the bottom of the layer.

*b. Melting layer parameters*

Melting layer microphysics is quantitatively analyzed by using various melting layer parameters defined at the top and bottom of the melting layer. The top of the melting layer is defined as a height of the maximum curvature in the  $Z$  profile (Drummond et al. 1996). The snow reflectivity expressed in equivalent reflectivity factor ( $Z_{e_{snow}}$ ) is an averaged  $Z$  value (in order to reduce the noise) over two successive range gates above the top of the melting layer (Fig. 8). The bottom of the melting layer is also determined at the height of the maximum curvature in the  $Z$  profile. The rain reflectivity also expressed in equivalent reflectivity factor ( $Z_{e_{rain}}$ ) is taken as an

averaged value over three successive range gates below the bottom of the melting layer. The basic eight parameters,  $H_{top}$ ,  $H_{bottom}$ ,  $H_{peak}$ ,  $Z_{e_{snow}}$ ,  $Z_{e_{peak}}$ ,  $Z_{e_{rain}}$ ,  $W_{snow}$ , and  $W_{rain}$ ; and their extended parameters,  $\gamma$ ,  $\Delta Z = Z_{e_{peak}} - Z_{e_{rain}}$ , and  $\Delta H = H_{top} - H_{bottom}$ , are estimated during the 0530-0648 UTC period when the  $Z$  profiles had distinct curvatures. The parameter  $\gamma$  is defined as the ratio of the products of  $Z$  and  $W_{dop}$  at the top ( $H_{top}$ ) and bottom ( $H_{bottom}$ ) of the melting layer (Drummond et al. 1996) by

$$\gamma = \frac{Z_{e_{snow}} W_{snow}}{Z_{e_{rain}} W_{rain}}, \quad (6)$$

where  $Z_{e_{snow}}$  and  $Z_{e_{rain}}$  are the equivalent reflectivity factor ( $\text{mm}^6 \text{m}^{-3}$ ) and  $W_{snow}$  and  $W_{rain}$  are the mean Doppler velocity of snow and rain at the top and bottom of the melting layer, which are shown in Fig. 9a. We assume a one-to-one relationship of the snowflake mass entering the melting layer and the raindrop mass leaving it, implying an absence of aggregation and breakup in the melting layer. Therefore, the deviation of the ratio of the two masses from unity indicates aggregation or breakup in the melting layer.

Aggregation and breakup-dominant periods are determined by using smaller  $\gamma$  values and larger  $\gamma$  values, respectively. Drummond et al. (1996) suggested a threshold of  $\gamma = 0.23$  to separate aggregation and breakup-dominant periods. Additional reflectivity constraints of  $Z_{e_{peak}} > 49$  dBZ and  $Z_{e_{rain}} > 38.3$  dBZ are used for reliably determining aggregation-dominant periods since  $Z_{e_{peak}}$  and  $Z_{e_{rain}}$  tend to be proportional to the degree of aggregation. In this study, the period (0600 to 0608 UTC, a time when  $H_{peak}$  descends as shown in Fig. 9a) is identified in order to examine the relationship of the descending bright band with the microphysics below the melting layer. In Fig. 9b, breakup is suggested over a limited time period between 0612 and 0618 UTC when  $\gamma$  values are largest, and aggregation is suggested for the other times. It is shown that the dominance of

breakup or aggregation is solely determined by the  $Z$  ratio at the two levels. For breakup-dominant periods, the  $Z$  ratio is relatively higher due to smaller  $Z_{e_{rain}}$  than for aggregation-dominant periods when smaller  $\gamma$  values are due to higher  $Z_{e_{rain}}$ . It is found that the Doppler velocity ratio is inversely proportional to the  $Z$  ratio during aggregation-dominant periods, indicating that snow aggregates are probably denser, more rimed, and even larger in size.

*c. Quantitative analysis*

In Fig. 10a, the scatterplot of  $Z_{e_{peak}}$  with bright band height ( $H_{peak}$ ) and thickness ( $\Delta H$ ) shows that  $\Delta H$  is proportional to  $Z_{e_{peak}}$  (Fabry and Zawadzki 1995; Klaassen 1988) but  $H_{peak}$  is inversely proportional to  $Z_{e_{peak}}$ . During breakup-dominant periods,  $\Delta H$  is especially small. The inverse relationship is probably due to melting-driven cooling because the downward propagation of cooled air would lower the bright band height as indicated in Durden et al. (1997). Fig. 10a shows that the average  $\Delta H$  for aggregation-dominant periods is about 30% larger than that for breakup due to melting of large snow particles at long fall distance.

Fig. 10b shows a slightly positive correlation between  $\Delta Z$  and  $Z_{e_{peak}}$ , and a negative correlation between  $\Delta Z$  and  $Z_{e_{rain}}$ . Both  $Z_{e_{peak}}$  and  $Z_{e_{rain}}$  are larger and less scattered for aggregation-dominant periods than those for breakup. Since all  $\Delta Z$  values (9.5-15 dB) in Fig. 10b are greater than 7 dB, the threshold that Huggel et al. (1996) used following Fabry and Zawadzki (1995) to discriminate weak and well-defined bright bands, the bright band within this TC is classified as strong and well-defined throughout the 80 min analysis period. For breakup-dominant periods, the average  $\Delta Z$  value is 2 dB larger than that for aggregation periods. This is due to a large reduction of  $Z_{e_{rain}}$  at the bottom of the melting layer that contributes more to an increase in  $\Delta Z$ , indicating active breakup in the lower half of the melting layer during breakup-

dominant periods. In this study,  $\Delta Z$  for breakup-dominant periods is larger (ranging from 11 to 15 dB) than aggregation-dominant periods (ranging from 10 to 13 dB). However, the large  $\Delta Z$  does not necessarily indicate the dominance of breakup because both periods have  $\Delta Z$  which includes the range of 11-13 dB. Thus, the parameter  $\Delta Z$  alone cannot be used for diagnosing the aggregation or breakup dominance, especially for the strong bright band case. On the whole, the average  $\Delta Z$  and  $\Delta H$  during the descending bright band period are between those during aggregation- and breakup-dominant periods, implying that the microphysical properties would be between the two distinguishable periods.

In Fig. 11a, the rain rate ( $R$ ) retrieved from the SAM shows positive correlations with both the  $Z_{e_{peak}}$  and  $\Delta H$ , particularly during aggregation-dominant periods. That is,  $R$  is proportional to bright band intensity. Since bright band intensity is highly dependent on the characteristics of the largest particles (Stewart et al. 1984), this is attributed to stronger precipitation produced by melting of larger snow aggregates over a longer fall distance (Fabry and Zawadzki 1995). In Fig. 11b, overall  $R$  shows little dependence on  $H_{peak}$ , indicating that for a given  $H_{peak}$ , there can be a wide range of  $R$ . Thus, a higher  $H_{peak}$  does not always imply a higher  $R$  (or larger  $\Delta H$ ). However, it is shown that the larger  $R$  during aggregation-dominant periods corresponded to lower  $H_{peak}$ , compared to other  $R$ - $H_{peak}$  pairs. A primary cause for this is melting-driven cooling that plays a role in lowering  $H_{peak}$  (Durdan et al. 1997) and producing negative buoyancy for downdrafts at, rather small temporal and spatial scales. It seems that the large scale variation in  $H_{peak}$  is probably more associated with other physical factors like temperature change, vertical air motion, etc. besides melting-driven cooling.

*d. Raindrop size distributions*

Fig. 12 shows the time-height sections of  $Z$ ,  $R$ ,  $D_m$ , and  $N_0$ . As proportional to  $Z$ , it is evident that  $R$  is higher during aggregation-dominant periods when the bright band was strong. Overall,  $D_m$  tends to be inversely proportional to  $R$  above 2 km AGL, and it is proportional to  $R$  below 2 km, particularly during aggregation-dominant periods.  $R$  is positively correlated with  $N_0$ , indicating that the increase in  $R$  is related to narrow spectra having a large number of small raindrops, thereby increasing the RSD slope and decreasing  $D_m$ . The notable increase in  $N_0$  particularly below 2 km AGL is attributed to raindrop breakup. (Evaporation would be small, given the nearly saturated sounding.) During aggregation-dominant periods,  $Z$  profiles are nearly uniform or decrease with height, indicating that collision-coalescence produces moderate to large raindrops and balances or even dominates over breakup (around 0540 and 0640 UTC). It appears that breakup is more dominant than collision-coalescence when  $R$  increases as  $D_m$  decreases, but collision-coalescence is more dominant than breakup when  $R$  increases as  $D_m$  also increases, intermittently shown below 2 km AGL. During the descending bright band period, both  $Z$  and  $R$  are smaller than those during aggregation-dominant periods. During this period, the slight increase in  $Z$  with decreasing height, along with a slightly larger  $D_m$  and smaller  $N_0$  indicates a relative increase in the number of moderate to large drops. Relatively stronger mesoscale downdrafts were measured below 2 km AGL during this period. Evaporation may decrease the number of smaller drops the most and collection of large and midsize drops may increase. Both the sporadic increase in  $R$  and  $D_m$  below 2 km AGL probably indicates the possibility of raindrop growth within the mesoscale downdrafts. On the other hand, during breakup-dominant periods, the smallest  $Z$  and  $D_m$  are shown among the sampling periods.

In Fig. 13, the correlation between  $R$  from the SAM and  $Z$ - $R$  relation ( $Z=367R^{1.3}$ , Tokay and Short 1996) shows better agreement when vertical air motions are included. The increase in  $R$

for a given  $Z$  in Fig. 13a is due to the fact that corrected downdrafts shift the spectrum to smaller fall speed and smaller drop diameter range. In Fig. 13a, the  $R$  derived from the  $Z$ - $R$  relation exceeds the SAM-retrieved  $R$  values. We interpret this as raindrops in this case are, on average, larger than those for a given  $Z$ . The inference of larger than average raindrops is consistent with the stronger bright band. In Fig. 13b, the overall underestimation in SAM-retrieved  $R$  is due to the absence of downward air motions which were estimated below the melting layer.

Fig. 14 shows the composite RSDs retrieved from the SAM model at 3472 m AGL during three periods. We chose this height closest to the bottom of the melting layer in order to minimize uncertainties or errors by horizontal advection of particles. Each RSD is an average of the five successive RSDs. The composite RSD during aggregation-dominant periods shows larger number concentrations at almost all drop sizes, corresponding to high reflectivity streaks shown in Fig. 12a. During breakup-dominant periods, the RSD shows a larger number of small drops and smaller number of large drops. This may be evidence of small raindrops resulting from melting of smaller snow particles produced by more active breakup in the melting layer. The RSD during the descending bright band shows smaller number concentrations at the small to midsize drop range when compared to those during the two other periods.  $D_m$  is a little larger during this period than during aggregation-dominant periods. The contributions of the number concentration of large drops on  $Z$  and  $D_m$  are relatively larger than at least those during breakup-dominant periods when  $D_m$  was smallest.

Since these composite RSDs were obtained near the bottom of the melting layer, the properties of snow size distributions near the top may be deduced from the RSDs. For aggregation-dominant periods, as expected, large snow aggregates were present just above the melting layer as aggregation dominates breakup within the melting layer, increasing the bright

band intensity. Small and dense rimed particles may be present as well in terms of large number concentration of small drops in Fig. 14 and large Doppler velocity ratio in Fig. 9b. During breakup-dominant periods, snow aggregates are expected to be relatively smaller and less dense. The smallest  $Z_{e_{rain}}$  suggests substantial breakup in the lower part of the melting layer during these periods. During the descending bright band period, presumably less efficient breakup within the melting layer and larger  $D_m$  indicates that on average, large and dense hydrometeors are probably present in terms of small  $\gamma$  values in Fig. 9b. However, their sizes seem to be smaller than those during aggregation-dominant periods since their  $Z_{e_{rain}}$  values are about 3 dB less.

## 6. Discussion

### a. Kinematics

Similar to this study, mesoscale up- and downdrafts above and below the melting layer in stratiform regions of hurricanes have been observed by Marks and Houze (1987) and Black et al. (1996). The mean range of  $w_{915}$  (-1 to 1.5 m s<sup>-1</sup>) in this study is larger than the mean  $w$  range of -0.3 to 1.3 m s<sup>-1</sup> from Marks and Houze (1987) and the mean  $w$  range of -0.5 to 1.0 m s<sup>-1</sup> in Fig. 8. of Black et al. (1996) in stratiform regions. Particularly, the mean downdraft velocity of -1 m s<sup>-1</sup> at low levels in this study is relatively large. It is likely that the strong downdrafts below the melting layer are overestimated by an underestimation of fall speeds of hydrometeors.

A convergence-divergence couplet within the melting layer has been documented in a limited number of papers (Cifelli et al. 1996; Mapes and Houze 1993, 1995; Steiner et al. 2003; Szeto et al. 1988; Szeto and Cho 1994). However, finding the convergence-divergence couplet within such an intense stratiform rainband of TC is unprecedented to our knowledge. Szeto and Stewart (1997) indicated that melting-driven cooling can produce mesoscale circulations that

enhance horizontal convergence around the melting layer. In this study, the convergence-divergence couplets both in the *div* profiles from both the Q-VAD and divergence theorem are probably indicative of cooling-induced circulations. (Although the couplet is not as obvious in the divergence theorem profile, the trend in strong convergence to weak convergence near the 4 km height is similar to that indicated in the Q-VAD profile.) The convergence above and divergence below the levels of  $Z$  maxima within the melting layer implies indirect fine-scale circulations of airflow as a coupling of the upper and lower half of the melting layer.

*b. Melting layer studies*

Huggel et al. (1996) used a  $\Delta Z$  threshold of 7 dB to determine weak or well-defined bright bands and showed a prominent negative correlation between  $\Delta Z$  and  $N_0$  particularly for the  $R$  range of 1-10 mm hr<sup>-1</sup>. However in this study, all  $\Delta Z$  values (9.5-15 dB) were greater than 7 dB and an overlapping range of  $\Delta Z$  was found for both the aggregation- and breakup-dominant periods. The average  $\Delta Z$  for breakup-dominant periods was 2 dB greater than that for aggregation-dominant periods. But the average  $Z_{e_{peak}}$  for aggregation was rather higher than that for breakup ( $\Delta Z = Z_{e_{peak}} - Z_{e_{rain}}$ ), suggesting that there are larger numbers of large particles (i.e., larger  $D_m$ , see Fig. 14) during aggregation-dominant periods. Therefore, one should exercise caution in interpreting the inverse relationship between  $\Delta Z$  and  $N_0$  (or  $A$ ), proposed by Huggel et al. (1996), if the bright band is strong with moderate precipitation. This is because a large  $\Delta Z$  does not always indicate a large number of large particles (i.e., small  $N_0$ ) as we found that the average  $\Delta Z$  was larger during breakup-dominant periods when  $D_m$  is comparatively smaller.

*c. Precipitation properties regarding bright band intensity*



During aggregation-dominant periods, the increase in number concentrations at all drop sizes was shown in Fig. 14. Such wide distributions have dependence on snow properties (size and habit) near the top of the melting layer. Yuter et al. (2006) indicated that the standard deviation of fall speeds of wet (i.e., partially melted) snow aggregates is larger than that of dry snow aggregates. The collision efficiency for aggregation-dominant periods would be higher due to the larger standard deviations of fall speeds of wet snow aggregates. A higher  $R$  during aggregation-dominant periods (Fig. 12b) as proportional to  $Z$  implies higher collection efficiency since  $R$  increases as the number concentration of large drops increases (Hu 1995; Low and List 1982). Considering that the largest factor to the decrease in  $Z$  below the melting layer is raindrop breakup (Stewart et al. 1984), a slow increase in  $Z$  and  $D_m$  with decreasing height suggests that moderate to large raindrops are still produced while breakup proceeds, even within the mesoscale downdrafts that were present below the melting layer throughout the analysis period. The almost constant or slightly increasing  $Z$  CFAD (Fig. 7a) indicates the raindrop growth by collection (particularly below 2 km AGL), suggesting relatively less breakup and evaporation in this particular stratiform rainband. During the descending bright band period (i.e., strong downdraft period), the collection efficiency is probably not as large as that during aggregation-dominant period due to smaller  $Z_{e_{rain}}$  and smaller numbers of small and large drops. However, relative to aggregation-dominant periods, evaporation associated with the strong downdrafts may come to play a more important role in decreasing  $R$  near the surface during the descending bright band period.

It is found that the effects of mesoscale downdrafts cannot be neglected for interpreting all dynamics and microphysics in and below the melting layer, particularly for intense stratiform

rainbands of TCs as in this case study. Therefore, the accurate estimation of  $w$  is more significantly required for this case. Even though the  $w$  variation would be larger with shorter periods (about 80 min) and the  $Z-V_f$  relations for snow and rain might not work well just below and above the melting layer,  $w$  from the profiler and the SAM showed good agreement. The RSD retrievals from the non-zero  $w$  assumption gave rise to less errors or biases than from the zero  $w$  assumption.

Errors in determining the top and bottom heights and the parameter values (for example,  $\gamma$ ) based on these levels can lead to false interpretation. Since the determination of snow and rain levels using the reflectivity curvatures can never be perfect, a secondary constraint such as the Doppler velocity would be auxiliary to make the levels be more accurate. Also, one should keep in mind that an increase of breakup in this study is a relative increase over aggregation within the melting layer, even during breakup-dominant periods.

## 7. Conclusions

This study examined the kinematic and microphysical characteristics of an unusually intense stratiform rainband within Tropical Storm Gabrielle. Mesoscale updrafts and downdrafts with an average range of  $-1$  to  $+1.5 \text{ m s}^{-1}$  were relatively strong. During a short analysis period of about 80 min, the rainband exhibited more variability in  $w$  and  $div$  profiles, compared with previous studies. The important findings from this study are as follows.

(i) The prominent convergence-divergence couplet both from the Q-VAD and divergence theorem implies the existence of prominent cooling-induced fine-scale circulations near the melting layer, primarily due to melting of large snow aggregates in association with strong bright band intensity.

Near-zero or positive divergence beneath the narrow convergence peak is probably representative of a physical behavior to satisfy a mass balance in the vertical.

(ii) It is the levels of reflectivity maxima where convergence above and divergence below is approximately separated and a minimum of spectral width is located, suggesting smallest breakup and largest snow aggregates within the melting layer.

(iii) Rainfall estimates retrieved from the SAM under the non-zero  $w$  assumption increase with  $Z_{e_{peak}}$  and bright band intensity, particularly during aggregation-dominant periods. A higher  $R$  as proportional to  $Z$  implies higher collection efficiency since  $R$  increases as the number concentration of large drops increases. Strong precipitation under strong bright band intensity is produced by melting of large snow aggregates over a long fall distance.

(iv) Rainfall estimates at the bottom of the melting layer show a positive relation with  $\Delta H$ , but less dependence on  $H_{peak}$ . However, the higher  $R$  during aggregation-dominant periods corresponded to lower  $H_{peak}$ . This is probably associated with melting-driven cooling that plays a principal role in lowering  $H_{peak}$  during this period, rather in small temporal and spatial scale. The large scale variation in  $H_{peak}$  is probably more associated with other physical factors like temperature change, vertical air motion, etc. except melting-driven cooling.

(v) The almost uniform  $Z$  CFAD below the melting layer indicates the balance between raindrop growth by collection and breakup/evaporation. This feature, in turn, implies a possibility of raindrop growth even within strong mesoscale downdrafts which were persistently measured

below 2 km AGL. In support of this, a slight increase in  $Z$  and  $D_m$  with decreasing height suggests that large and midsize raindrops are produced while breakup advances. However, breakup and evaporation are probably more effective than collection close to the ground particularly during strong downdraft periods.

Aggregation and riming contributions to bright band intensity are related to vertical profiles of temperature, relative humidity, cloud water content, and  $w$  around the melting layer. Hence, collocated thermodynamic soundings along with high-resolution  $Z$  measurements are necessary for in-depth bright band studies. Since the RSDs near the bottom of the melting layer show a close connection with bright band intensity (i.e., aggregation degree), this study proposes an implication of retrieving snow size distributions near the top of the melting layer using the relationship between fall speeds, masses, and size spectra of snow and rain suggested by Leary and Houze (1979). The possibility of a wind profiler application into melting layer studies (i.e., the small-scale variations in precipitation, airflow, and heating/cooling, especially around the melting layer) is significantly reemphasized in this study. To build up quantitatively generalized relations of the melting layer parameters with precipitation properties, other case studies with more radar data will be conducted in the near future.

### *Acknowledgements*

This research was sponsored by the National Science Foundation under grant ATM-0533596 and by the National Oceanic and Atmospheric Administration under grant NA06OAR4600156.

## References

- Atlas, D., R. C. Srivastava, and R. S. Sekhon, 1973: Doppler radar characteristics of precipitation at vertical incidence. *Rev. Geophysics. Space Phys.*, **11**, 1-35.
- Barthazy, E., W. Henrich, and A. Waldvogel, 1998: Size distribution of hydrometeors through the melting layer. *Atmospheric research*, **47-48**, 193-208.
- Barnes, G. M., E. J. Zipser, D. Jorgensen, and F. Marks Jr., 1983: Mesoscale and convective structure of a hurricane rainband. *J. Atmos. Sci.*, **40**, 2125–2137.
- Beard, K. V., 1985: Simple altitude adjustments to raindrop velocities for Doppler radar analysis. *J. Atmos. Oceanic Technol.*, **2**, 468-471.
- Biggerstaff, M. I., L. J. Wicker, J. Guynes, C. Ziegler, J. M. Straka, E. N. Rasmussen, A. Doggett IV, L. D. Carey, J. L. Schroeder, and C. Weiss, 2005: The shared mobile atmospheric research and teaching radar: A collaboration to enhance research and teaching. *Bulletin of the American Meteorological Society*, **86**, 1263–1274.
- Black, M. L., R. W. Burpee, and F. D. Marks, 1996: Vertical motion characteristics of tropical cyclones determined with airborne Doppler radial velocities. *J. Atmos. Sci.*, **53**, 1887–1909.
- Cifelli, R., S. A. Rutledge, D. J. Boccippio, and T. Matejka, 1996: Horizontal divergence and vertical velocity retrievals from Doppler radar and wind profiler observations. *J. Atmos. Oceanic Technol.*, **13**, 948–966.
- Cifelli, R., Christopher R. Williams, Deepak K. Rajopadhyaya, Susan K. Avery, Kenneth S. Gage, and P. T. May, 2000: Drop-size distribution characteristics in tropical mesoscale convective systems. *J. Appl. Meteor.*, **39**, 760–777.
- Drummond, F. J., R.R. Rogers, S.A. Cohn, W.L. Ecklund, D.A. Carter, and J.S. Wilson, 1996:

- A new look at the melting layer. *J. Atmos. Sci.*, **53**, 759–769.
- Durden, L. S., A. Kitiyakara, E. Im, A. B. Tanner, Z. S. Haddad, F. K. Li, and W. J. Wilson, 1997: ARMAR observations of the melting layer during TOGA COARE. *IEEE transactions on geoscience and remote sensing*, **35**, 6, 1453-1456.
- Fabry, F., and I. Zawadzki, 1995: Long-term radar observations of the melting layer of precipitation and their interpretation. *J. Atmos. Sci.*, **52**, 838–851.
- Gamache, J. K., R. A. Houze Jr., and F. D. Marks Jr., 1993: Dual-aircraft investigation of the inner core of Hurricane Norbert. Part III: Water budget. *J. Atmos. Sci.*, **50**, 3221–3243.
- Houze, R. A. Jr., 1989: Observed structure of mesoscale convective systems and implications for large-scale heating. *Quart. J. Roy. Meteor. Soc.*, **115**, 425–461.
- Hu, Z., 1995: The role of raindrop coalescence and breakup in rainfall modeling. *Atmospheric Research*, **37**, 343-359.
- Huggel, A., W. Schmid, and A. Waldvogel, 1996: Raindrop size distributions and the radar bright band. *J. Appl. Meteor.*, **35**, 1688–1701.
- Janssen, L. H., and G. A. Van der Spek, 1985: The shape of Doppler spectra from precipitation. *IEEE Trans. Aerosp. Electron. Syst.*, vol. AES-21, 208-219.
- Klaassen, W., 1988: Radar observations and simulation of the melting layer of precipitation. *J. Atmos. Sci.*, **45**, 3741–3753.
- Knupp, K. R., J. Walters, and M. Biggerstaff, 2006: Doppler profiler and radar observations of boundary layer variability during the landfall of Tropical Storm Gabrielle. *J. Atmos. Sci.*, **63**, 234–251.
- Lawrence, M., and R. Blake, 2002: Preliminary Report: Hurricane Danny 16–26 July 1997. National Hurricane Center, 18 pp.

- Leary, C. A., and R. A. Houze Jr., 1979: Melting and evaporation of hydrometeors in precipitation from anvil clouds of deep tropical convection. *J. Atmos. Sci.*, **36**, 669–679.
- Low, T. B., and R. List, 1982: Collision, coalescence and breakup of raindrops. Part I: Experimentally established coalescence efficiencies and fragment size distributions in breakup. *J. Atmos. Sci.*, **39**, 1591–1606.
- Mapes, B., and R. A. Houze, 1993: Integrated view of the 1987 Australian monsoon and its mesoscale convective systems. II: Vertical structure. *Q. J. R. Meteorol. Soc.*, **119**, 733–754.
- Mapes, B., and R. A. Houze, 1995: Diabatic divergence profiles in western pacific mesoscale convective system. *J. Atmos. Sci.*, **52**, 1807–1828.
- Marks, F. D., and R. A. Houze, 1987: Inner core structure of Hurricane Alicia from airborne Doppler radar observations. *J. Atmos. Sci.*, **44**, 1296–1317.
- Matejka, T., and R. C. Srivastava, 1991: An improved version of the extended velocity azimuth display analysis of single-Doppler radar data. *J. Atmos. Oceanic Technol.*, **8**, 453–466.
- Molinari, J., P. Dodge, D. Vollaro, K. L. Corbosiero, and F. Marks, 2006: Mesoscale aspects of the downshear reformation of a tropical cyclone. *J. Atmos. Sci.*, **63**, 341–354
- Rajopadhyaya, D. K., P. T. May, R. C. Cifelli, S. K. Avery, C. R. Williams, W. L. Ecklund and K. S. Gage, 1998: The effect of vertical air motions on rain rates and median volume diameter determined from combined UHF and VHF wind profiler measurements and comparisons with rain gauge measurements. *J. Atmos. Oceanic Technol.*, **15**, 1306–1319.
- Powell, M. D., 1990: Boundary layer structure and dynamics in outer hurricane rainbands.

- Part II: Downdraft modification and mixed layer recovery. *Mon. Wea. Rev.*, **118**, 918–938.
- Schumacher, C., and R. A. Houze, 2003: Stratiform rain in the tropics as seen by the TRMM precipitation radar. *Journal of Climate*. **16**, 1739–1756.
- Srivastava, R. C., 1987: A model of intense downdrafts driven by the melting and evaporation of precipitation. *J. Atmos. Sci.*, **44**, 1752–1773.
- Steiner, M., O. Bousquet, R. A. Houze, Jr., B. F. Smull, and M. Mancini, 2003: Airflow within major Alpine River Valleys under heavy rainfall. *Quart. J. Roy. Meteor. Soc.*, **129**, 411–431.
- Stewart, R. E., J. D. Marwitz, J. C. Pace, and R. E. Carbone, 1984: Characteristics through the melting layer of stratiform clouds. *J. Atmos. Sci.*, **41**, 3227–3237.
- Szeto, K. K., and H. R. Cho, 1994: A numerical investigation of squall lines. Part I: The control experiment. *J. Atmos. Sci.*, **51**, 414–424.
- Szeto, K. K., and R. E. Stewart, 1997: Effects of melting on frontogenesis. *J. Atmos. Sci.*, **54**, 689–702.
- Szeto, K. K., A. L. Charles, and R. E. Stewart, 1988: Mesoscale circulations forced by melting snow. Part I: Basic simulations and dynamics. *J. Atmos. Sci.*, **45**, 1629–1641.
- Tokay, A., and D. Short, 1996: Evidence from tropical raindrop spectra of the origin of rain from stratiform versus convective clouds. *J. Appl. Meteor.*, **35**, 355–371.
- Tokay, A., D. A. Short, C. R. Williams, W. L. Ecklund, and K. S. Gage, 1999: Tropical rainfall associated with convective and stratiform clouds: Intercomparison of disdrometer and profiler measurements. *J. Appl. Meteor.*, **38**, 302–320.
- Ulbrich, C. W., and P. B. Chilson, 1994: Effects of variations in precipitation size distribution and fallspeed law parameters on relations between mean Doppler fallspeed and reflectivity factor. *J. Atmos. Oceanic Technol.*, **11**, 1656–1663.



- Williams, C. R., 2002: Simultaneous ambient air motion and raindrop size distributions retrieved from UHF vertical incident profiler observations. *Radio Sci.*, **37**, IO.1029/2000RS002603.
- Willis, P. T., and A. J. Heymsfield, 1989: Structure of the melting layer in mesoscale convective system stratiform precipitation. *J. Atmos. Sci.*, **46**, 2008–2025.
- Yang, B., W. Yuqing, and B. Wang, 2007: The effect of internally generated inner-core asymmetries on tropical cyclone potential intensity. *J. Atmos. Sci.*, **64**, 1165–1188.
- Yokoyama, T., H. Tanaka, K. Akaeda, T. Ohtani, N. Yoshizawa, M. Yamanaka, A. Mita, Y. Ishizaka, and A. Ono, 1985: Observation on microphysical processes in the stratiform precipitations including melting layers at Mt. Fuji. *J. Meteor. Soc. Japan*, **63**, 100-111.
- Yuter, S. E., and R. A. Houze, Jr., 1995: Three-dimensional kinematic and microphysical evolution of Florida cumulonimbus, Part II: Frequency distributions of vertical velocity, reflectivity, and differential reflectivity. *Mon. Wea. Rev.*, **123**, 1941-1963.
- Yuter, S. E., D. Kingsmill, L. B. Nance, and M. Löffler-Mang, 2006: Observations of precipitation size and fall speed characteristics within coexisting rain and wet snow. *Journal of Applied Meteorology and Climatology*, **45**, 1450–1464.
- Zawadzki, I., W. Szyrmer, C. Bell, and F. Fabry, 2005: Modeling of the melting layer. Part III: The density effect. *J. Atmos. Sci.*, **62**, 3705–3723.

## Figure captions

Figure 1. Horizontal plane of reflectivity at 3.5 km AGL from the TBW radar at 065614 UTC on 14 September 2001. The stratiform rainband considered in this study extends from the left-center to the right-center part of the figure. The red circle shows the location of the TBW radar and the thick black line represents the land boundary.

Figure 2. Vertical sections along  $x = 0$  of radar reflectivity (dBZ) (panels a and c) and radial Doppler velocity ( $\text{m s}^{-1}$ ) (panels b and d) at 060105 and 065614 UTC from the WSR-88D radar at Tampa Bay (KTBW). The arrow at  $y=0$  km represents the location of the SMART-R and MIPS. The bottom panel shows a horizontal plane of reflectivity with horizontal wind vectors (storm-relative) over it on 065614 UTC at 3.5 km AGL. The wind vectors were acquired by dual Doppler radar process using the CEDRIC software. Upper and lower circles show the locations of the TBW and SMART-R, respectively.

Figure 3. Upper-air soundings at 0000 (left) and 0600 UTC (right) at KTBW on 14 September 2001.

Figure 4. Time-height sections of (a) radar reflectivity (dBZ), (b) Doppler velocity ( $\text{m s}^{-1}$ ), and (c) spectral width ( $\text{m s}^{-1}$ ) derived from the 915-MHz profiler.

Figure 5. Time-height sections of vertical air motions (a) from the EVAD and (b) the 915-MHz profiler. The horizontal line in panel (a) shows the top of the section (b) at the same scale for the comparison and the dashed line shows the approximate level of the  $0.0 \text{ m s}^{-1}$  contour.

Figure 6. Composite profiles of (a) horizontal divergence and (b) vertical air motions derived from various methods between 0545 and 0631 UTC. For (a), the thin line the EVAD divergence profile, the thick line the Q-VAD divergence profile, and the middle thick line represent the divergence profile from the theorem. A three-point running average with regard to heights was performed for Q-VAD and the divergence theorem. For (b), each vertical air motion profile derived from EVAD (thin), the divergence theorem (middle thick), Q-VAD (thick), and the reflectivity-fall speed relations (dashed) is shown. The vertical air motions derived from the reflectivity-fall speed relations were also three-point smoothed. The horizontal line at 4.8 km shows the approximate top of the melting layer.

Figure 7. CFADs (Contoured Frequency by Altitude Diagrams) for (a) reflectivity (bin: 1.25 dB), (b) Doppler velocity (bin:  $0.25 \text{ m s}^{-1}$ ), (c) spectral width (bin:  $0.15 \text{ m s}^{-1}$ ), and (d) wind speed (bin:  $1.0 \text{ m s}^{-1}$ ) during the 0530-0648 UTC. The top horizontal line at 4.8 km represents the approximate top of the melting layer and  $0^\circ\text{C}$  level. The bottom horizontal line at 3.47 km shows a height where the SAM performed for the RSD retrievals.

Figure 8. Schematic diagram for the parameters (See the text for more details).

Figure 9. (a) Time-height section of the reflectivity near the bright band region. The black-colored pixels represent reflectivity greater than 50 dBZ. The thick solid line indicates  $H_{peak}$  and upper and lower thin lines indicate  $H_{top}$  and  $H_{bottom}$ , respectively. The symbols of rectangle and circle represent the breakup and aggregation-dominant periods, respectively. (b) Time variations of the  $\gamma$  parameter (solid line), reflectivity ratio (dashed line), and Doppler velocity ratio (dotted line). The circle and rectangle symbols represent aggregation- and breakup-dominant periods, respectively. The triangles indicate the period of a prominent decrease in bright band height. The horizontal line indicates the threshold of 0.23 (suggested by Drummond et al. 1996).

Figure 10. (a) Scatterplot is between  $Z_{e_{peak}}$  and the bright band height (top, left axis) and bright band thickness (bottom, right axis). (b) Scatterplot is between  $\Delta Z$  and  $Z_{e_{peak}}$  (top) and  $Z_{e_{rain}}$  (bottom). The symbols are as defined in Fig. 9b with solid dots representing all other observations.

Figure 11. (a) Scatterplot is between rain rate ( $\text{mm hr}^{-1}$ ) and  $Z_{e_{peak}}$  (top, left axis), and  $\Delta H$  (bottom, right axis). (b) Scatterplot is between rain rate and  $H_{peak}$ . Rain rate is retrieved at 3472 m AGL. The symbols are as defined in Figs. 9b. and 10.

Figure 12. Figure 12. Time-height sections of (a) reflectivity (dBZ), (b) rain rate ( $\text{mm hr}^{-1}$ ), (c)  $D_m$  (mm), and (d)  $N_0$  ( $\text{m}^{-3} \text{mm}^{-1}$ ). For each section, the smoothing using the eight nearest values was performed in time and height. The symbols are as defined in Fig. 9b.

Figure 13. (a) Comparison between  $R$  ( $\text{mm hr}^{-1}$ ) from the SAM with vertical air motion accounted, and  $Z$ - $R$  relation and (b) the comparison  $R$  ( $\text{mm hr}^{-1}$ ) from the SAM with vertical air motion not accounted, and  $Z$ - $R$  relation.

Figure 14. Comparison of the averaged RSDs during the three major periods at 3472 m AGL. The black solid line represents the RSD during the first aggregation-dominant periods (0548 UTC), the red line the RSD during the breakup-dominant periods, and the blue line the RSD during the descending BB height periods. The thick lines are those retrieved from the SAM model with vertical air motion accounted and the thin lines are those from the measured profiler spectra. The number in bracket indicates the mean mass-weighted diameter (mm).

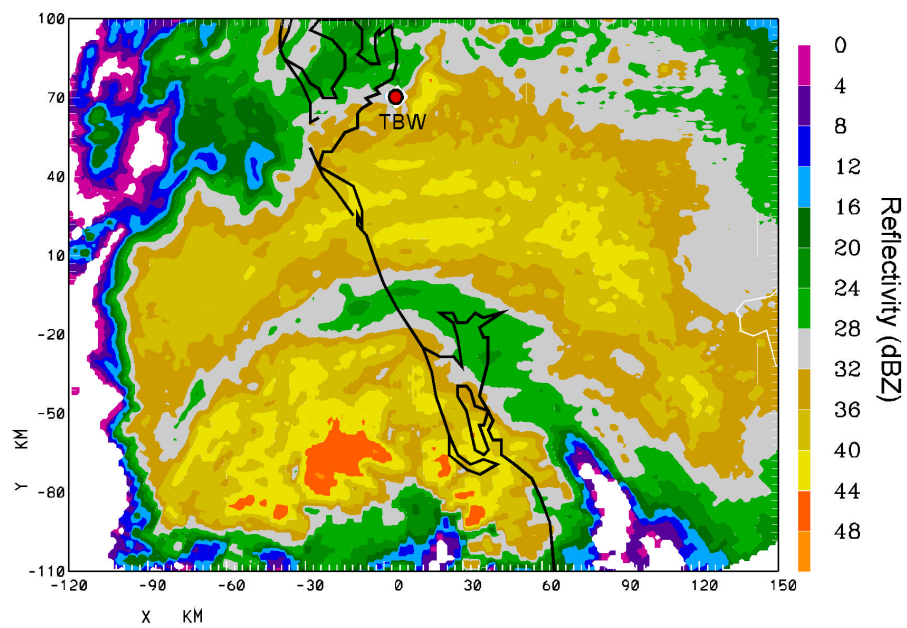


Figure 1. Horizontal plane of reflectivity at 3.5 km AGL from the TBW radar at 065614 UTC on 14 September 2001. The stratiform rainband considered in this study extends from the left-center to the right-center part of the figure. The red circle shows the location of the TBW radar and the thick black line represents the land boundary.

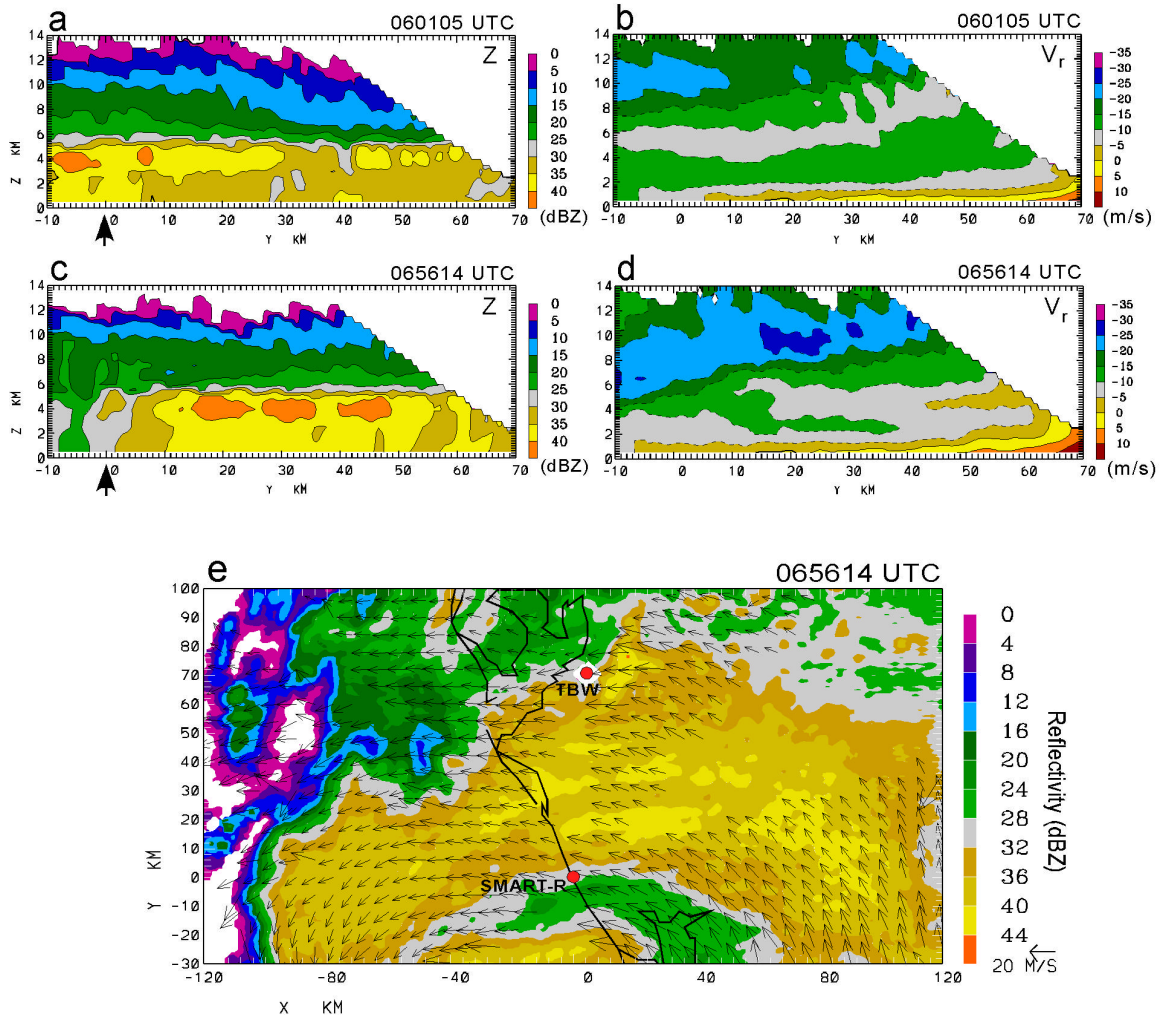


Figure 2. Height-range sections of radar reflectivity (dBZ) ((a), (c)) and radial Doppler velocity ( $\text{m s}^{-1}$ ) ((b), (d)) at 060105 and 065614 UTC from the WSR-88D radar at Tampa Bay (KTBW). The arrow at  $y=0$  km represents the location of the SMART-R and MIPS. The bottom panel shows a horizontal plane of reflectivity with horizontal wind vectors (storm-relative) over it on 065614 UTC at 3.5 km AGL. The wind vectors were acquired by dual Doppler radar process using the CEDRIC software. Upper and lower circles show the locations of the TBW and SMART-R, respectively.

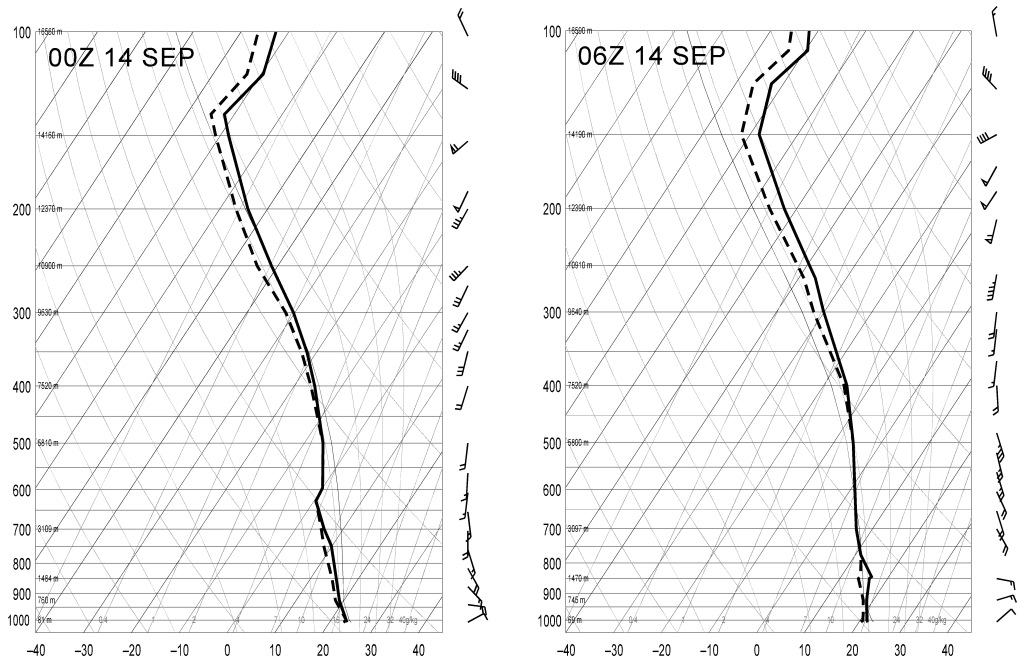


Figure 3. Upper-air soundings at 0000 (left) and 0600 UTC (right) at KTBW on 14 September 2001.



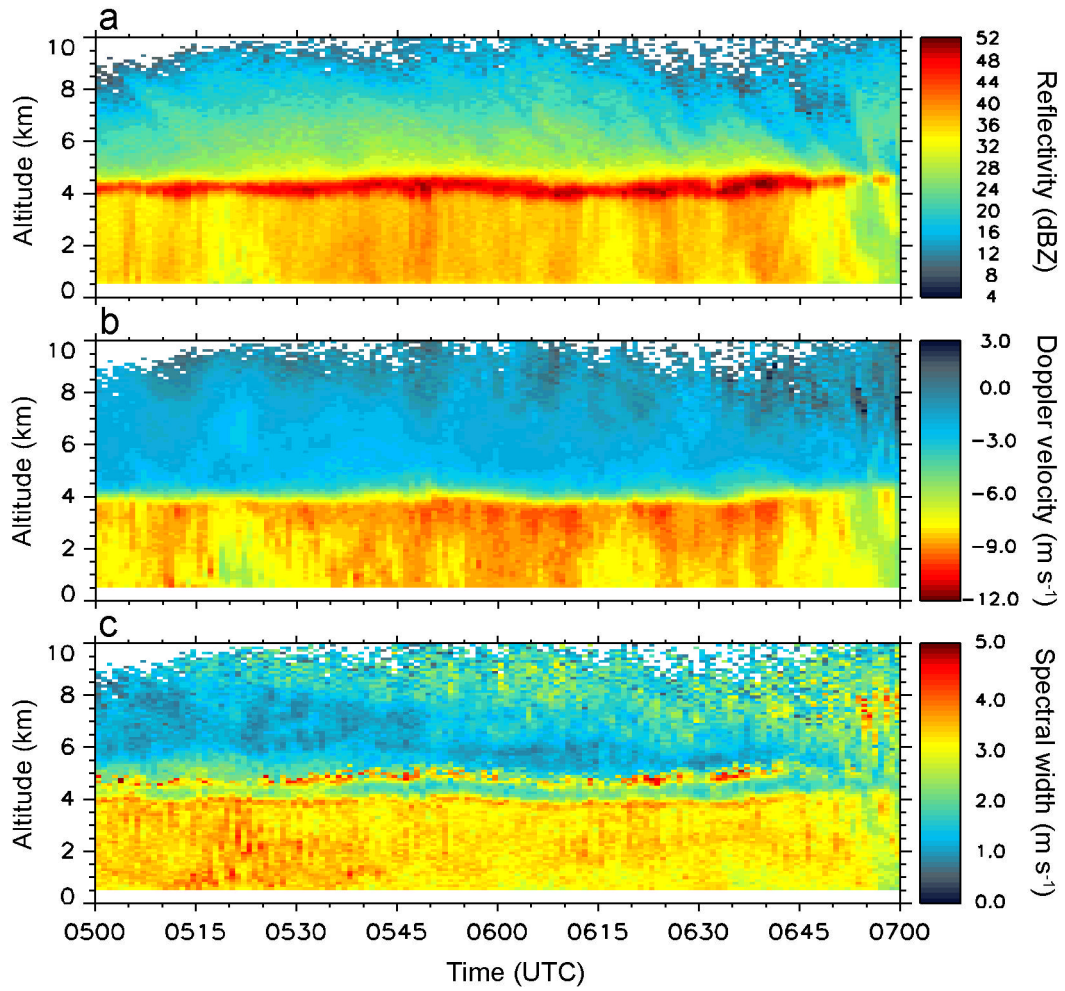


Figure 4. Time-height sections of (a) radar reflectivity ( $\text{dBZ}$ ), (b) Doppler velocity ( $\text{m s}^{-1}$ ), and (c) spectral width ( $\text{m s}^{-1}$ ) derived from the 915-MHz profiler.

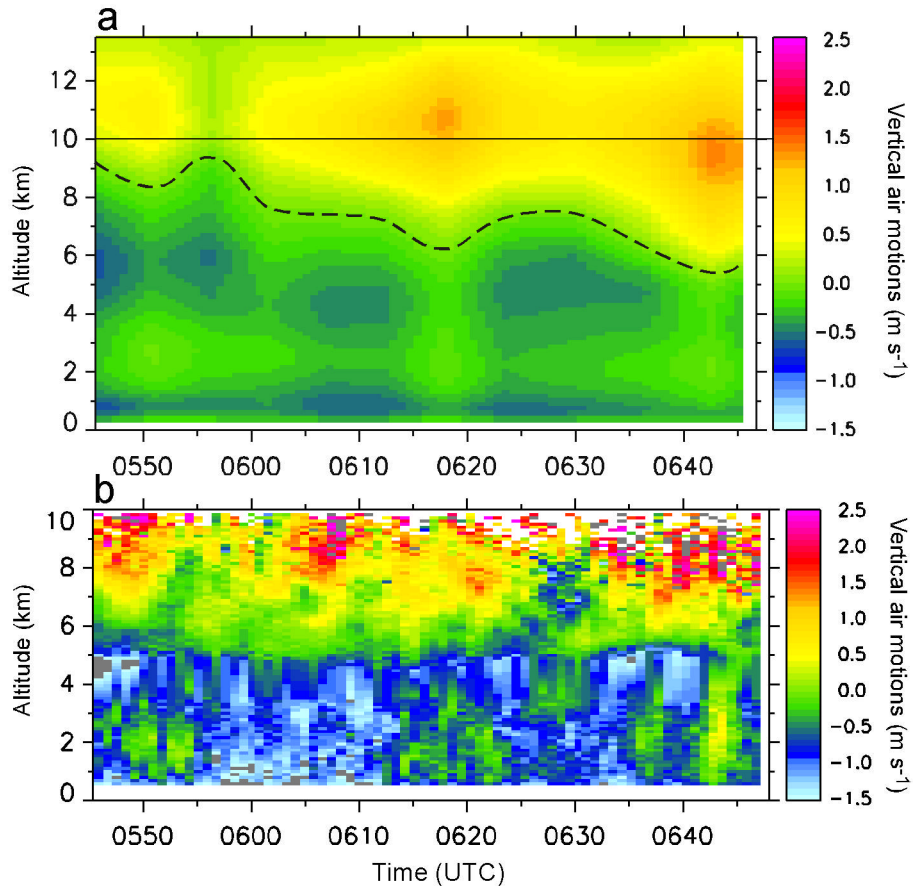


Figure 5. Time-height sections of vertical air motions (a) from the EVAD and (b) the 915-MHz profiler. The horizontal line in panel (a) shows the top of the section (b) at the same scale for the comparison and the dashed line shows the approximate level of the  $0.0 \text{ m s}^{-1}$  contour.

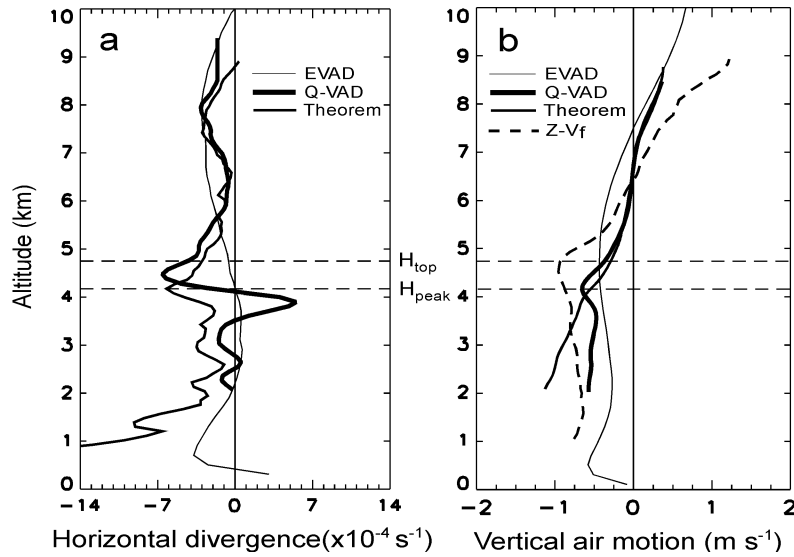


Figure 6. Composite profiles of (a) horizontal divergence and (b) vertical air motions derived from various methods between 0545 and 0631 UTC. For (a), the thin line the EVAD divergence profile, the thick line the Q-VAD divergence profile, and the middle thick line represent the divergence profile from the theorem. A three-point running average with regard to heights was performed for Q-VAD and the divergence theorem. For (b), each vertical air motion profile derived from EVAD (thin), the divergence theorem (middle thick), Q-VAD (thick), and the reflectivity-fall speed relations (dashed) is shown. The vertical air motions derived from the reflectivity-fall speed relations were also three-point smoothed. The horizontal line at 4.8 km shows the approximate top of the melting layer.

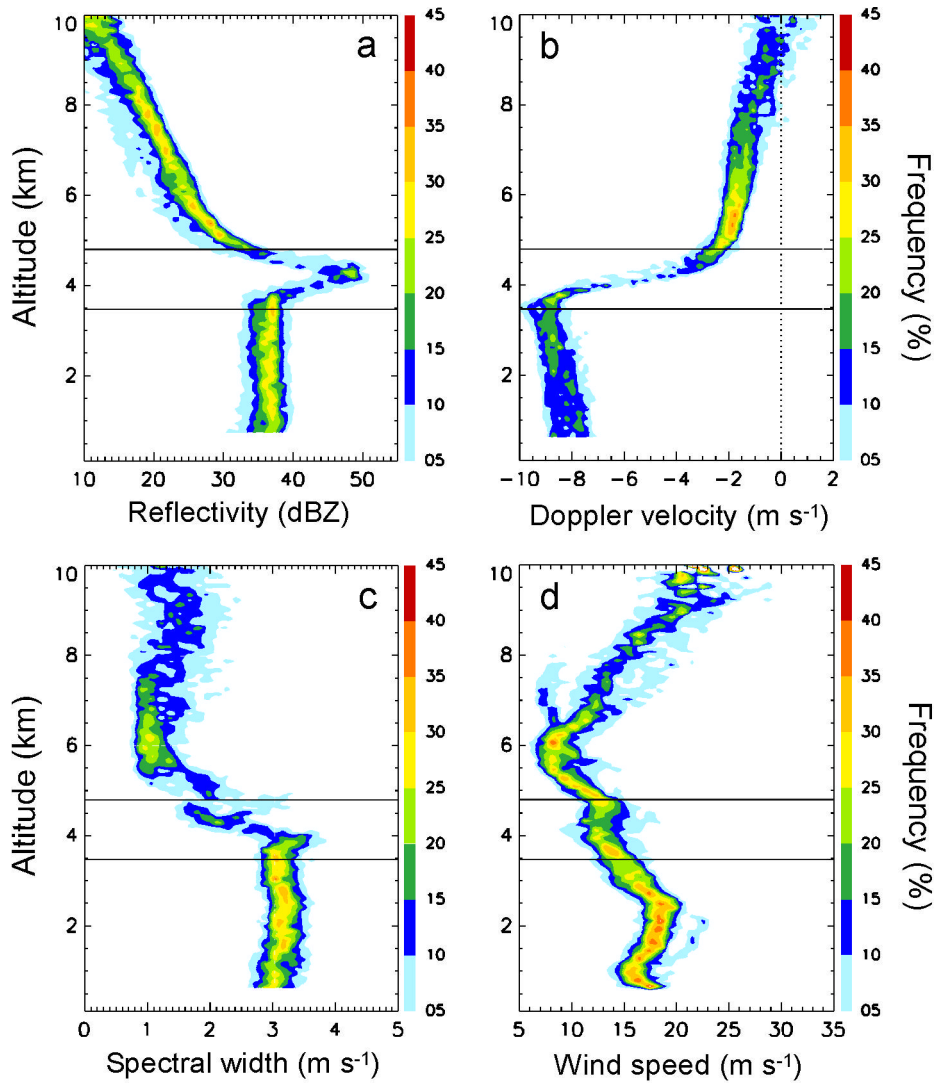


Figure 7. CFADs (Contoured Frequency by Altitude Diagrams) for (a) reflectivity (bin: 1.25 dB), (b) Doppler velocity (bin: 0.25  $\text{m s}^{-1}$ ), (c) spectral width (bin: 0.15  $\text{m s}^{-1}$ ), and (d) wind speed (bin: 1.0  $\text{m s}^{-1}$ ) during the 0530-0648 UTC. The top horizontal line at 4.8 km represents the approximate top of the melting layer and 0°C level. The bottom horizontal line at 3.47 km shows a height where the SAM performed for the RSD retrievals.

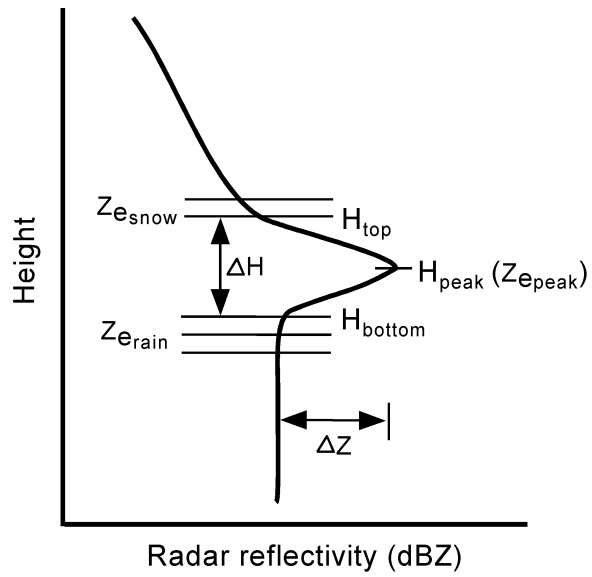


Figure 8. Schematic diagram for the parameters (See the text for more details).

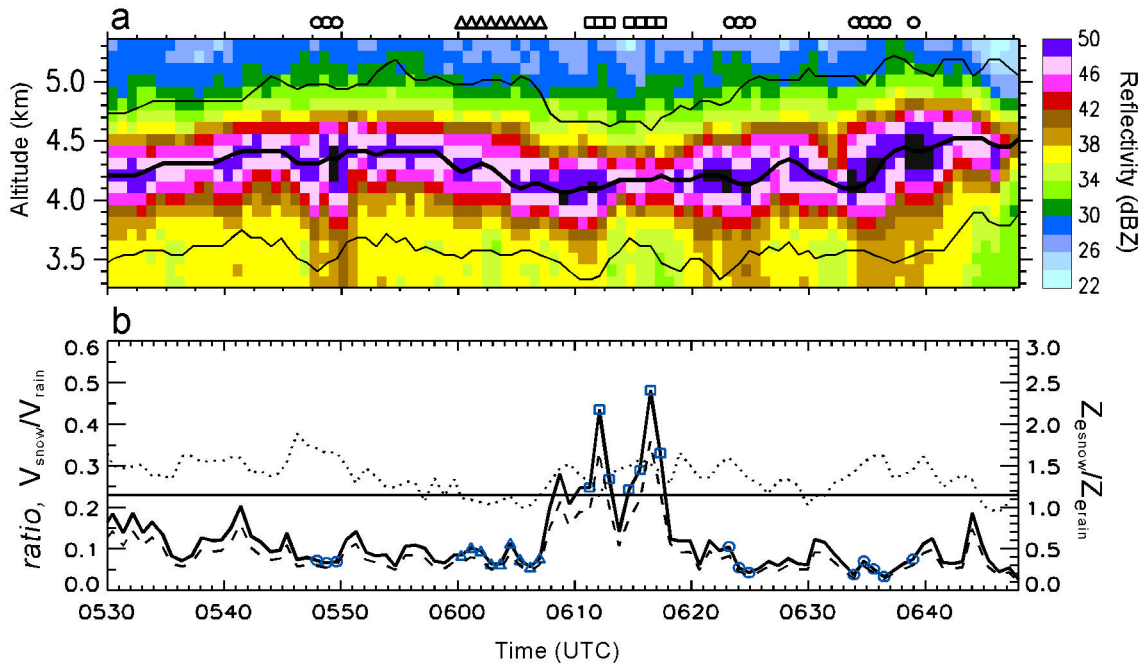


Figure 9. (a) Time-height section of the reflectivity near the bright band region. The black-colored pixels represent reflectivity greater than 50 dBZ. The thick solid line indicates  $H_{peak}$  and upper and lower thin lines indicate  $H_{top}$  and  $H_{bottom}$ , respectively. The symbols of rectangle and circle represent the breakup and aggregation-dominant periods, respectively. (b) Time variations of the  $\gamma$  parameter (solid line), reflectivity ratio (dashed line), and Doppler velocity ratio (dotted line). The circle and rectangle symbols represent aggregation- and breakup-dominant periods, respectively. The triangles indicate the period of a prominent decrease in bright band height. The horizontal line indicates the threshold of 0.23 (suggested by Drummond et al. 1996).

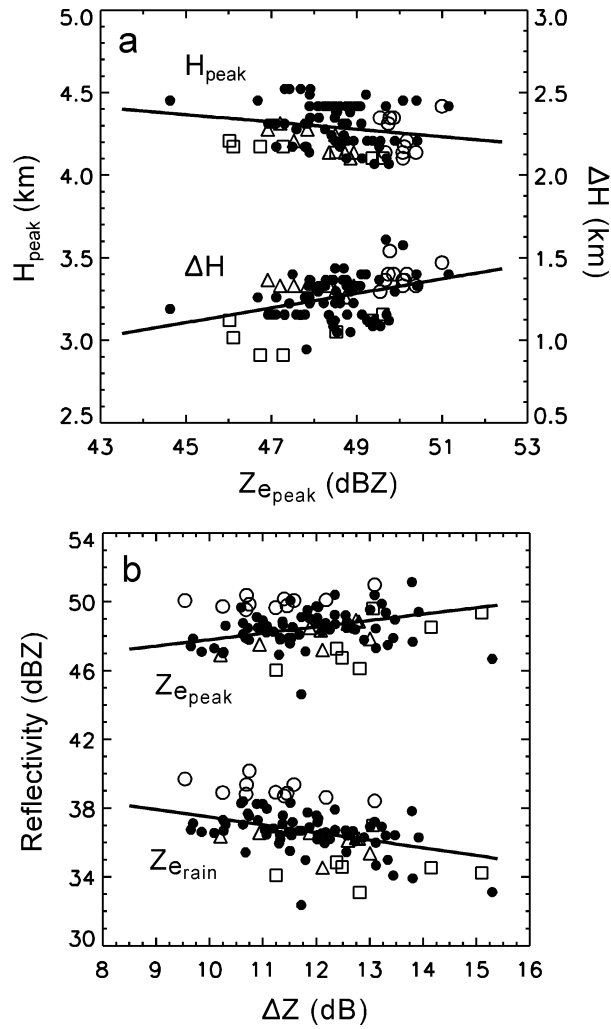


Figure 10. (a) Scatterplot is between  $Z_{e_{peak}}$  and the bright band height (top, left axis) and bright band thickness (bottom, right axis). (b) Scatterplot is between  $\Delta Z$  and  $Z_{e_{peak}}$  (top) and  $Z_{e_{rain}}$  (bottom). The symbols are as defined in Fig. 9b with solid dots representing all other observations.

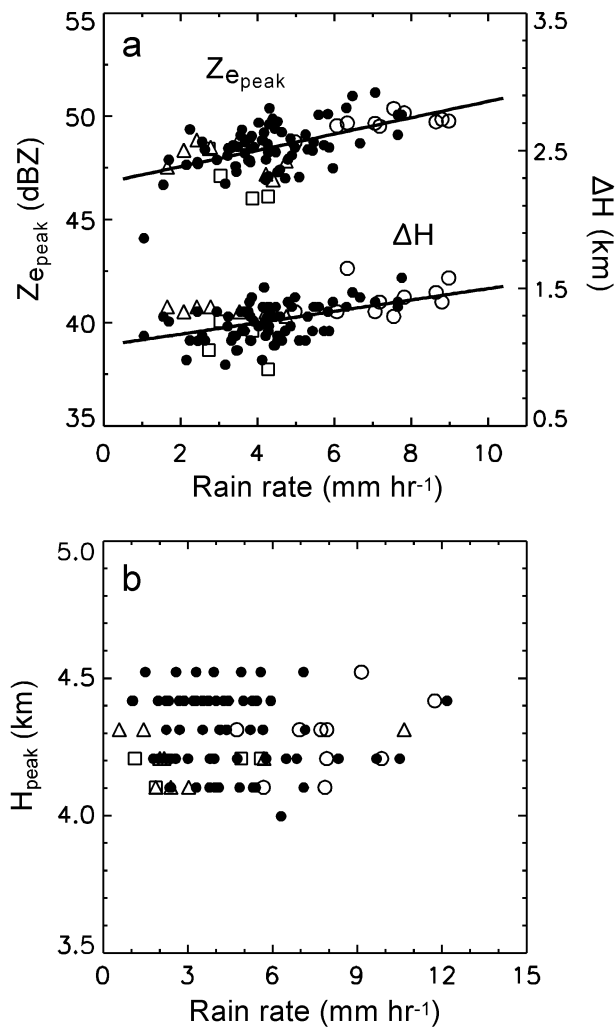


Figure 11. (a) Scatterplot is between rain rate (mm hr<sup>-1</sup>) and  $Z_{e_{peak}}$  (top, left axis), and  $\Delta H$  (bottom, right axis). (b) Scatterplot is between rain rate and  $H_{peak}$ . Rain rate is retrieved at 3472 m AGL. The symbols are as defined in Figs. 9b and 10.



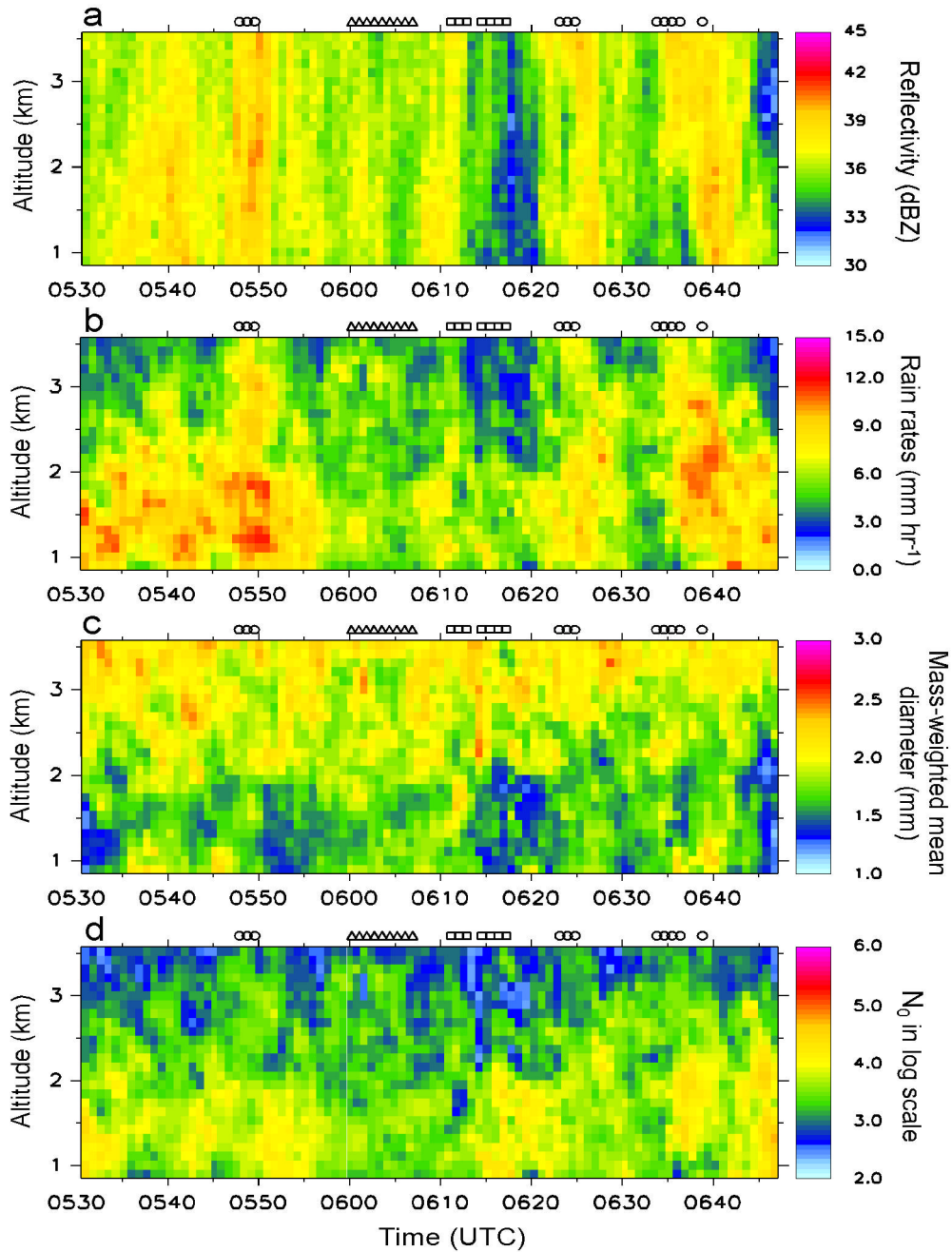


Figure 12. Time-height sections of (a) reflectivity (dBZ), (b) rain rate (mm hr<sup>-1</sup>), (c)  $D_m$  (mm), and (d)  $N_0$  (m<sup>-3</sup> mm<sup>-1</sup>). For each section, the smoothing using the eight nearest values was performed in time and height. The symbols are as defined in Fig. 9b.

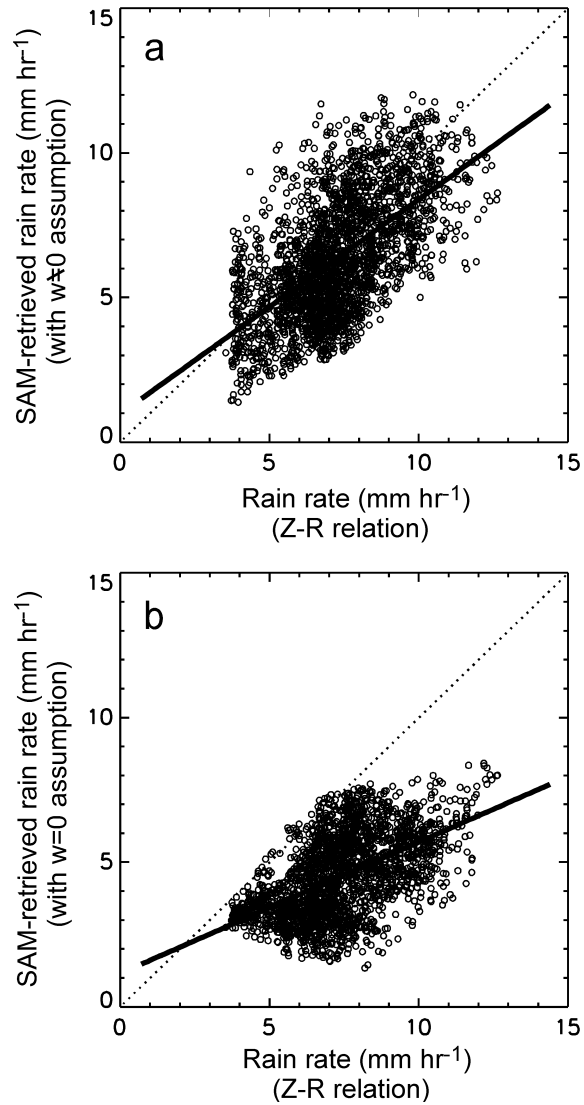


Figure 13. (a) Comparison between  $R$  (mm hr<sup>-1</sup>) from the SAM with vertical air motion accounted, and  $Z$ - $R$  relation and (b) the comparison  $R$  (mm hr<sup>-1</sup>) from the SAM with vertical air motion not accounted, and  $Z$ - $R$  relation.

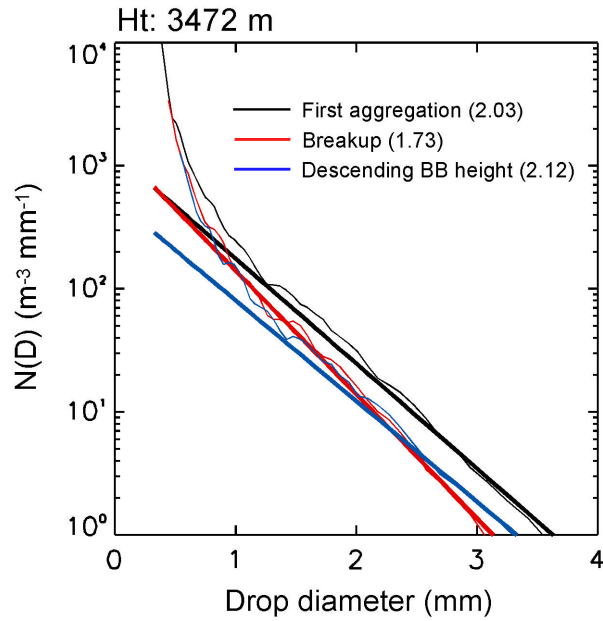


Figure 14. Comparison of the averaged RSDs during the three major periods at 3472 m AGL. The black solid line represents the RSD during the first aggregation-dominant periods (0548 UTC), the red line the RSD during the breakup-dominant periods, and the blue line the RSD during the descending BB height periods. The thick lines are those retrieved from the SAM model with vertical air motion accounted and the thin lines are those from the measured profiler spectra. The number in bracket indicates the mean mass-weighted diameter (mm).